THE ASTROPHYSICAL JOURNAL, 342:860–870, 1989 July 15

SPECTROSCOPIC IMAGES OF NGC 7027 IN THE NEAR-INFRARED DUST EMISSION FEATURES

C. E. WOODWARD,[1,2] JUDITH L. PIPHER,[1] MARK SHURE,[1,3] AND W. J. FORREST
Department of Physics and Astronomy, University of Rochester

AND

K. SELLGREN[1]
Institute for Astronomy, University of Hawaii
Received 1988 September 2; accepted 1988 December 19

ABSTRACT

The spatial relationships between the distribution of ionized gas and the "unidentified" 3–12 μm infrared dust-feature emission yield important clues as to the identification of candidate grain/molecule materials responsible for feature emission and provide observational constraints useful in the evaluation of proposed feature emission mechanisms. Here we present isophote maps derived from spatially resolved ($\sim 0''.42$ pixel^{-1}), moderate spectral resolution ($\Delta\lambda/\lambda \sim 1\%$) images of the planetary nebula NGC 7027 in the 3.28 μm and 3.4 μm "unidentified" emission features, and in the Brα (4.052 μm) hydrogen recombination line. Comparison of these images clearly shows that the 3.28 μm emission is spatially more extended than the ionized gas. Analysis and modeling of the spatial distribution of the 3.28 μm feature strength suggest that roughly equal amounts of feature emission appear to come from within the H II region and from a shell outside the H II region. The spatial distribution of the 3.4 μm feature emission is found to be similar to that of the 3.28 μm feature emission.

Subject headings: infrared: spectra — interstellar: grains — nebulae: individual (NGC 7027) — nebulae: planetary

I. INTRODUCTION

The spatial distribution of the unidentified infrared (henceforth UIR) dust emission features in astrophysical sources provides insight into the emission processes, the formation and destruction processes, and the wavelength range of feature-exciting photons, and it constrains identification of possible candidate feature-emitting materials. Comparison of the spatial distribution and intensity of the UIR emission to tracers of the ionized gas component, as deduced from radio continuum maps, observations of the hydrogen recombination lines, or ionic fine-structure lines, permits investigation of possible correlations between UIR feature strength and nebular excitation critical to assessment of both the proposed feature-exciting materials and the emission mechanism. From thermal dust continuum ($\lambda \geq 3$ μm) observations, one can assess whether the spatial distribution of the UIR feature-emitting material is associated with that of the continuum-emitting component.

Recently, attention has focused on small, isolated polycyclic aromatic hydrocarbon (PAH) macro-molecule/small grains (Allamandola, Tielens, and Barker 1985; Leger and Puget 1984) as the origin of the UIR emission. Although theoretical PAH spectra are in modest agreement with astronomical spectra, alternative emission materials exist. Other competing models include emission from quenched carbonaceous composites (QCCs) (Sakata *et al.* 1984) and hydrogenated amorphous carbons (HACs) (Duley and Williams 1986; Borghesi, Bussoletti, and Colangeli 1987). In each of these models, emission at 3.28 μm is attributed to a —CH stretch mode (1–0), probably from a hydrocarbon with an aromatic structure, while emission at 3.4 μm may arise from the (2–1) vibrational mode (Barker, Allamandola, and Tielens 1987) or from the (1–0) —CH stretch in a linear hydrocarbon (Sakata *et al.* 1984). Emission at 11.3 μm is tentatively identified with an out-of-the-plane bending mode of the same —CH structure.

The proximity (940 pc; Masson 1986) and high surface brightness of NGC 7027, especially in the 3.28 μm and 3.4 μm emission features (Cohen *et al.* 1986; Merrill, Soifer, and Russell 1975), make it an ideal candidate for high-spatial resolution imaging observations at near-infrared wavelengths with moderate spectral resolution. This paper presents isophote maps derived from $0''.42$ pixel^{-1}, $\sim 1\%$ spectral resolution images of NGC 7027 in the 3.28 μm and 3.4 μm UIR emission features, and in the Brα (4.052 μm) hydrogen recombination line, as well as in adjacent continua.

II. OBSERVATIONS

The near-infrared spectroscopic observations of NGC 7027 reported here were obtained on the NASA IRTF 3 m telescope in 1986 August with the University of Rochester 1–5 μm infrared CCD array camera (Forrest *et al.* 1985). For these observations the camera was equipped with a two-segment circular variable filter wheel (CVF) with a measured equivalent width (approximately Gaussian profile) of $\simeq 1.0\%$, and a FWHP of $\sim 0.95\%$. In addition, broad-band images at H (1.65 μm), K (2.2 μm), L' (3.75 μm), M' (4.67 μm), and at $\lambda = 3.26$ μm with a narrow-band filter ($\Delta\lambda = 0.2$ μm) were obtained; discussion of these latter images can be found in Woodward (1987) or Woodward *et al.* (1989*a*).

The observing techniques and data reduction procedures described in Woodward (1987) and Forrest *et al.* (1985) were employed. The plate scale and the rotation of the camera

[1] Visiting Astronomer at the NASA Infrared Telescope Facility, which is operated by the University of Hawaii under contract with the National Aeronautics and Space Administration.
[2] Now at Wyoming Infrared Observatory.
[3] Now at the Institute for Astronomy, University of Hawaii.

system were calibrated using star streaks (telescope drive turned off) and star pairs as described by Forrest, Pipher, and Stein (1986). The plate scale of the camera system for these observations was 0".42 pixel^{-1}, resulting in a total field of view of $\sim 13''.4 \times 13''.4$. Flux calibration was derived from observations of the standard stars α Lyr, γ Lyr, and BS 8143: we estimate an overall uncertainty of at most 10% in the absolute flux levels.

The continuum flux density at each feature/line peak wavelength was determined from an interpolation of adjacent continuum images for each pixel. Candidate continuum wavelengths were selected by examining the 2–4 μm spectrum of NGC 7027 (Merrill *et al.*), with the criteria that the continuum wavelengths (3.18 μm and 3.70 μm for the 3 μm features; 3.80 μm and 4.10 μm for Brα) avoid spectral regions near strong telluric absorption bands, and be at least 1 resolution element away from the feature/line wavelength centers. Determination of the correct continuum flux density at 3.4 μm is severely complicated by the presence of an emission "plateau" above an otherwise flat continuum from 3.2 to 3.6 μm (Nagata *et al.* 1988; Geballe *et al.* 1985). Although the intensity of the "plateau" emission as a function of spatial position in NGC 7027 is not known, we estimate that it introduces a $\sim 20\%$ uncertainty in the 3.4 μm flux. This estimate is based on a comparison of our estimated 3.4 μm continuum (in a $\sim 3''$ beam centered on the bright optical knot), which we derived from a linear interpolation between our chosen continuum points at 3.18 μm and 3.70 μm, to that estimated by Nagata *et al.* (1988) toward the same position in the nebula using a continuum defined by a local minimum in the spectrum at ~ 3.36 μm. The corresponding uncertainty in our derived 3.28 μm flux is estimated to be $\sim 2\%$.

To ensure accurate positional justification among different spectral images (e.g., 4.052 μm vs. 3.28 μm), sequential images in the line/feature or continuum wavelengths were obtained (within ≤ 70 s). Any subsequent positional uncertainty in aligning images, due to telescope drift or deliberate placement of the nebula on different areas on the array, was reconciled using these sequential "snapshots." This technique is required because there are no point sources in the field for alignment. The final positional uncertainty of a given image, relative to the other images, is less than or equal to 0".42.

The observed 3.28 μm and 3.4 μm feature flux densities and the Brα line flux density integrated over the central $8''.4 \times 8''.4$ of the nebula are given in Table 1. Also given in Table 1 are the dynamic range in the images (col. [3]) and the total on-source integration time (col. [4]). Since the FWHP of the UIR features ($\Delta\lambda$[3.28 μm] = 0.043 μm, $\Delta\lambda$[3.4 μm] = 0.028 μm, Nagata *et al.* 1988; Geballe *et al.* 1985) are greater than or equal to our CVF resolution at these wavelengths, we convolved our CVF transmission profile (assumed Gaussian) with the high-resolution ($\lambda/\Delta\lambda = 1400$–1700) 3 μm spectrum of NGC 7027 (Nagata *et al.* 1988) evaluated at the feature peak wavelength. Thus we estimate the factor, α, by which the actual feature-peak flux density is underestimated by our observations (α[3.28 μm] $\sim$ 1.39; α[3.4 μm] $\sim$ 1.45).

The UIR feature strengths (Table 1; col. [5]) are then estimated from Table 1; column (2) as $\alpha_\lambda F_\lambda \Delta\lambda$(FWHP), where $\Delta\lambda$(FWHP) are taken from the observations of Nagata *et al.* (1988). The Brα line is unresolved by our CVF, thus $\Delta\lambda$(4052 μm) was assumed to be equal to the CVF resolution. The total luminosity in the 3.28 μm emission band from our observations is $\sim 5.13 \pm 0.24\ L_\odot$, while the total luminosity in the 3.4 μm feature emission $\sim 0.86 \pm 0.26\ L_\odot$. The total 3 μm UIR feature luminosity accounts for less than 0.1% of the total infrared luminosity, $\sim 9.5 \times 10^3\ L_\odot$ (Natta and Panagia 1981).

We have not corrected the 3.28 μm feature strength for any contribution from the H I Pfδ recombination line emission, at $\lambda = 3.2961$ μm, present at the edge of the CVF bandpass centered at 3.28 μm. Adopting a ratio of Pfδ/Brα = 0.06 (Giles 1977; Brocklehurst 1971) and using the integrated Brα flux (Table 1; col. [5]) deduced from our image (Fig. 1*c*), the Pfδ line contributes less than or equal to 6% to the total observed 3.28 μm feature flux. This is in good agrement with the estimate of Geballe *et al.* (1985), $\sim 3\%$ contribution from the Pfδ line, or less than or equal to 9% contribution deduced from the observations of Nagata *et al.* (1988), where the Pfδ line and 3.28 μm peaks are partially resolved. Thus correcting the 3.28 μm image for Pfδ line emission was deemed unnecessary. However, Geballe *et al.* (1985) point out that in certain nebulae, such as IC 418, the (estimated) Pfδ line emission is greater than or equal to 50% of the observed intensity at 3.28 μm.

Contour maps of the continuum subtracted 3.28 μm and 3.4 μm feature-peak flux density are given in Figure 1*a* and Figure 1*b*, respectively. Figure 1*c* presents the contour map of the continuum subtracted Brα (4.052 μm) line-peak flux density. All figures are drawn to the same spatial scale. The filled circle (●) denotes the position (Cudworth and Orvecz 1978) of the

TABLE 1

FEATURE OR LINE FLUXES AND OBSERVATIONAL SUMMARY OF NGC 7027 INFRARED SPECTROSCOPIC IMAGES

λ (μm) (1)	Observed Continuum Subtracted Line or Feature Peak Flux Density[a] (10^{-16} W cm^{-2} μm^{-1}) (2)	Peak Signal/noise[b] (3)	Integration Time (s) (4)	Line or Feature Strengths[c] (10^{-17} W cm^{-2}) (5)
4.05 (Brα)	2.68 ± 0.20	75	83	1.18 ± 0.09
3.40	1.00 ± 0.09	47	172	0.39 ± 0.11
3.28	4.14 ± 0.18	102	150	2.47 ± 0.11

[a] Measured in an 8".4 octagonal aperture.

[b] Defined as the ratio of the average peak signal per pixel divided by the average rms noise per pixel.

[c] Measured in an 8".4 octagonal aperture. The Brα line width ($\Delta\lambda$) was assumed to be equal to the resolution of the filter. The 3.4 μm and 3.28 μm features strengths are estimated from col. (2) as $\alpha_\lambda F_\lambda \Delta\lambda$(FWHP), where α[3.28 μm] = 1.39, α[3.4 μm] = 1.45, (cf. § II in text) with $\Delta\lambda$(3.28 μm) = 0.043 μm, and $\Delta\lambda$(3.4 μm) = 0.027 μm (Nagata *et al.* 1988).

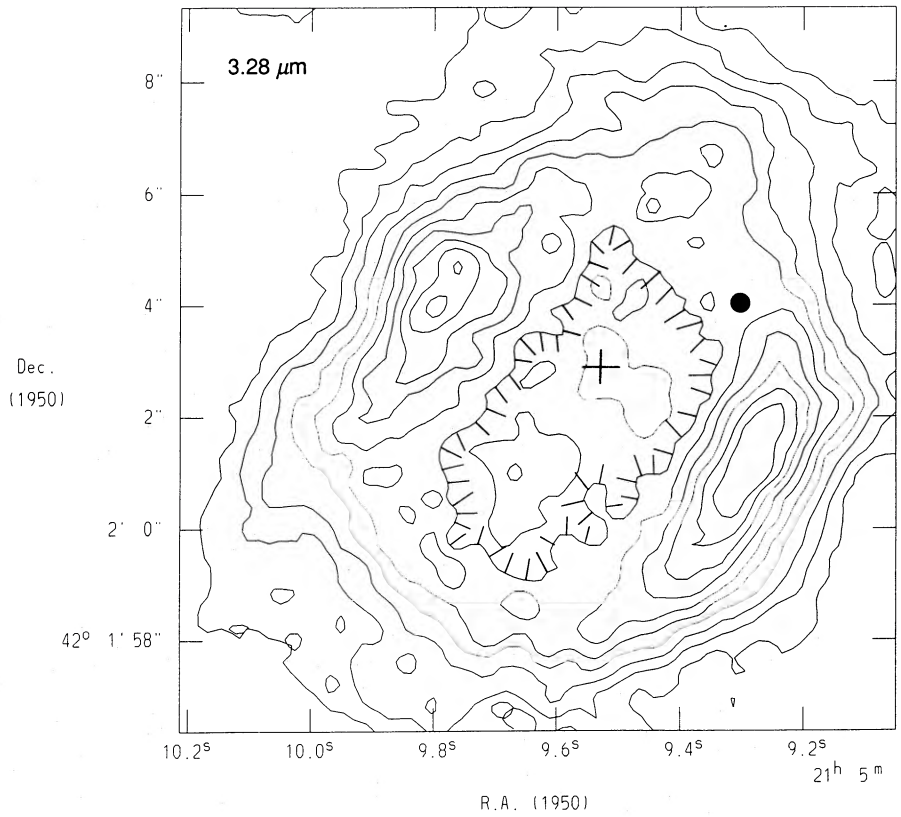

FIG. 1*a*

FIG. 1.—The flux density isophotes of NGC 7027 from near-infrared spectroscopic images obtained on the NASA IRTF 3 m telescope. The total field of view of each image is ~13.8 square seconds of arc, with each pixel subtending $\sim 4.1 \times 10^{-12}$ ster (~0".4 × 0".4). The " + " in each image designates the position of the 5 GHz continuum interferometric radio center (1950) = $21^h5^m9^s.53$, $\delta(1950) = 42°2'2".9$, while the approximate position of the bright optical knot (Cudworth and Orvecz 1978) is indicated by a filled circle (●). (*a*) Continuum subtracted 3.28 μm feature-peak flux density isophotes. The contour lines denote values from 1.75×10^{-18} W cm^{-2} μm^{-1} arcsec^{-2} to 3.33×10^{-17} W cm^{-2} μm^{-1} arcsec^{-2} at intervals 3.16×10^{-18} W cm^{-2} μm^{-1} arcsec^{-2}. The approximate 1 σ surface brightness in the image estimated from the rms noise per pixel at the periphery is $\sim 5.84 \times 10^{-19}$ W cm^{-2} μm^{-1} arcsec^{-2}. (*b*) Continuum subtracted 3.4 μm feature-peak flux density isophotes. The contour lines denote values from 1.58×10^{-18} W cm^{-2} μm^{-1} arcsec^{-2} to 9.13×10^{-18} W cm^{-2} μm^{-1} arcsec^{-2} at intervals 1.52×10^{-18} W cm^{-2} μm^{-1} arcsec^{-2}. The approximate 1 σ surface brightness in the image estimated from the rms noise per pixel at the periphery is $\sim 5.08 \times 10^{-19}$ W cm^{-2} μm^{-1} arcsec^{-2}. (*c*) The continuum subtracted Brα (4.052 μm) line-peak flux density isophotes. The contour lines denote values from 2.56×10^{-18} W cm^{-2} μm^{-1} arcsec^{-2} to 2.66×10^{-17} W cm^{-2} μm^{-1} arcsec^{-2} at intervals 2.41×10^{-18} W cm^{-2} μm^{-1} arcsec^{-2}. The approximate 1 σ surface brightness in the image estimated from the rms noise per pixel at the periphery is $\sim 8.6 \times 10^{-19}$ W cm^{-2} μm^{-1} arcsec^{-2}.

"bright knot" evident at optical wavelengths [α(1950) = $21^h5^m9^s.3$, δ(1950) = 42°2'04"]. The full width half-power (FWHP) diameter of NGC 7027 and the separation between intensity peaks along the major (PA = 150°) and minor axis (PA = 60°) of the nebula were determined from measurements of the intensity profiles (Figs. 2 and 3). These data are summarized in Table 2, as is the FWHP point spread function (along the same axes) determined from the observations of standard stars.

III. DISCUSSION

a) The 3.28 μm and 3.4 μm Spectroscopic Images

The observed spatial distributions of the 3.28 μm (Fig. 1*a*) and 3.4 μm (Fig. 1*b*) continuum-subtracted feature flux densities are quite similar in NGC 7027, although the 3.4 μm image is of lower signal-to-noise ratio due to the small feature-to-continuum contrast. Regions of peak feature strength at both wavelengths occur along the minor axis of the nebula

TABLE 2

PEAK SEPARATIONS AND FULL WIDTH HALF-MAXIMUM OF NGC 7027 IMAGES

WAVELENGTH (μm)	PEAK SEPARATION NGC 7027 POSITION ANGLE[a]		FWHP[a] NGC 7027 POINT SOURCE POSITION ANGLE			
	60°	150°	60°	150°	60°	150°
4.05	5.1	6.7	7.2	9.9	1.1	1.2
3.40	6.2	[b]	8.4	[b]	1.1	1.2
3.28	6.2	8.0	8.4	11.0	1.1	1.2
6 cm[c]	5.4	...	7.5	10.2	...	...

[a] In seconds of arc, determined from the minor axis (PA = 60°) and major axis (PA = 150°) intensity profiles passing through the center of the nebula at RA(1950) = $21^h5^m9^s.53$, Decl(1950) = 42°2'2".9. The FWHP of a point source was determined from observations of standard stars. The uncertainty in the measurements is ±0".1.

[b] No well-defined structure in the intensity profile is evident along this axis.

[c] From the radio observations of Masson 1986.

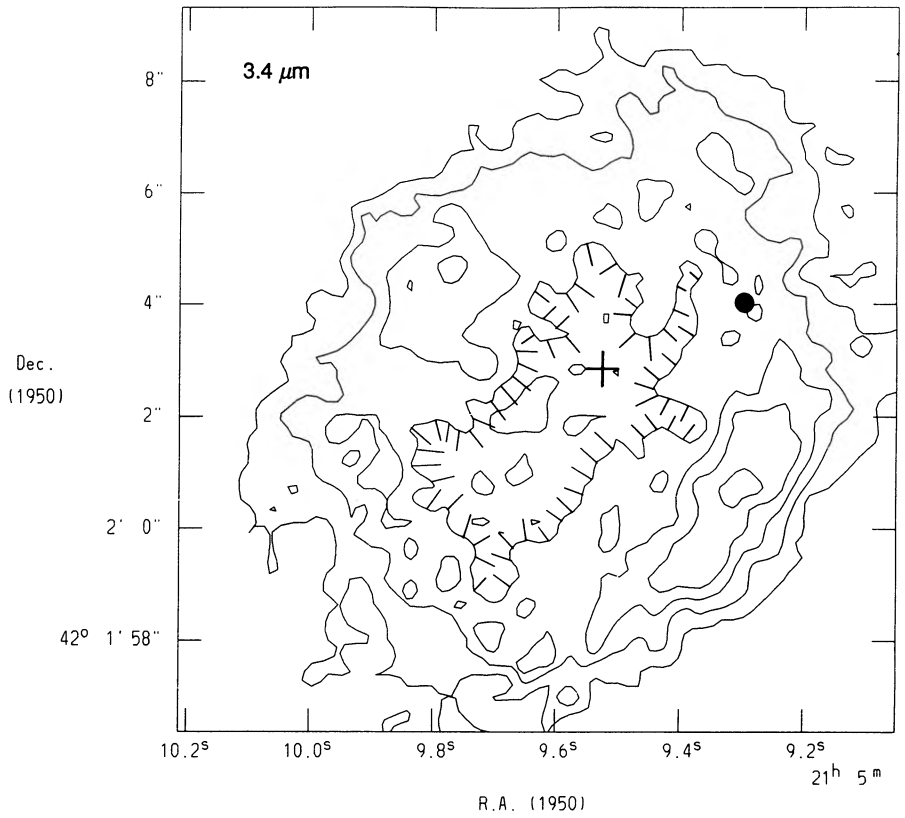

FIG. 1*b*

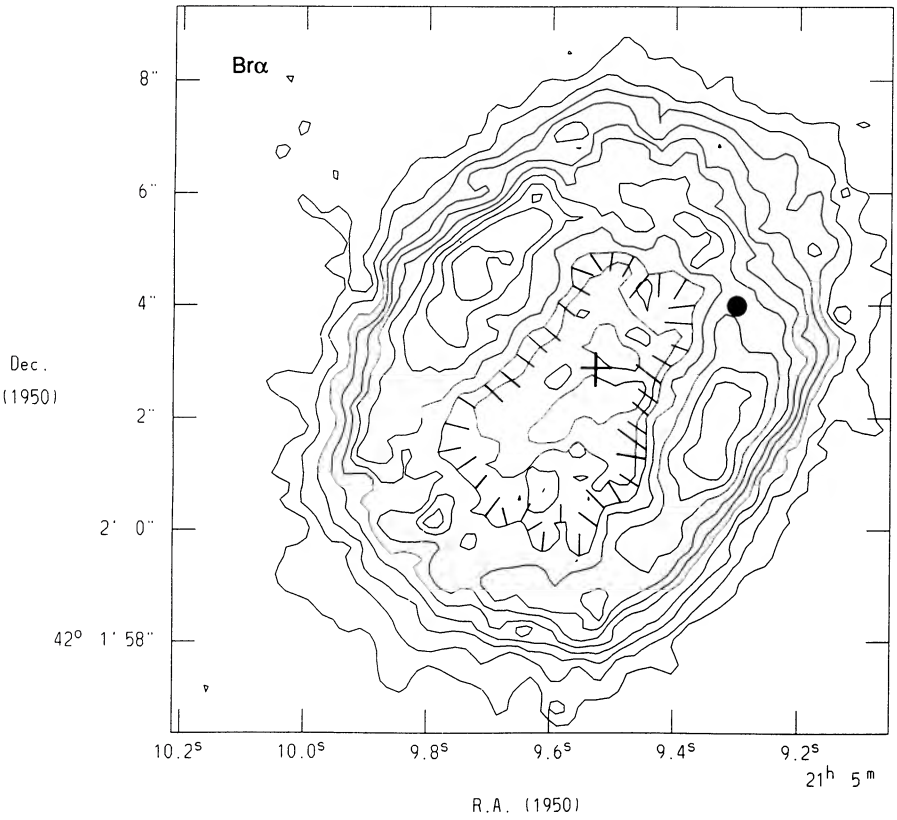

FIG. 1*c*

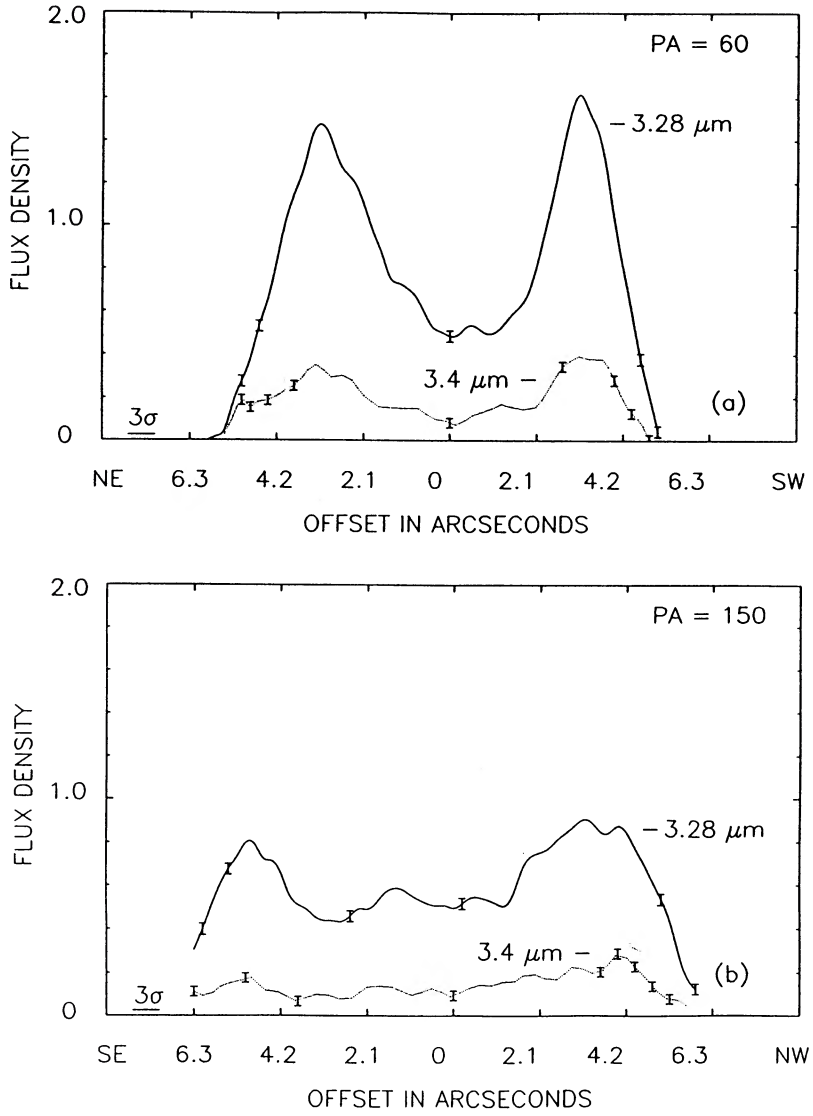

FIG. 2.—The continuum subtracted, feature-peak 3.28 μm and 3.4 μm flux density ($\times 4.4 \times 10^{-20}$ W cm^{-2} μm^{-1} arcsec^{-2}) intensity profile of NGC 7027 determined from the spectroscopic images obtained on the NASA IRTF 3 m telescope. (*a*) The intensity profiles as a function of position along the minor axis (PA = 60°) on a line passing through the center (0 offset position) of NGC 7027, $\alpha(1950) = 21^h5^m9^s.53$, $\delta(1950) = 42°2'2.9''$. The error bars represent the typical statistical ($\pm 1\ \sigma$) uncertainty in the determined continuum subtracted flux densities. (*b*) Same as Fig. 2*a* except along the major axis (PA = 150°). The horizontal bar in lower left of each figure is 3 σ for the 3.28 μm flux density.

(PA = 60°), while toward the nebular center a "hollow" of low surface brightness is evident.

The continuum-subtracted, peak 3.28 μm and 3.4 μm flux density intensity profiles are presented in Figure 2 as a function of position along the major and minor axes on a line passing through the center of NGC 7027, $\alpha(1950) = 21^h5^m9^s.53$, $\delta(1950) = 42°2'02''.9$. Along the minor axis of the nebula (Fig. 2*a*) the intensity maxima of the 3.28 μm and 3.4 μm emission are coincident and well-defined. In regions where 3.28 μm UIR emission is strong, the 3.4 μm UIR emission is also strong; indeed the feature strengths along the minor axis of the nebula are strongly correlated. The ratio of the integrated 3.28 μm to 3.4 μm continuum-subtracted flux (2″ × 2″ square aperture) toward five locations in the nebula is approximately constant, 6.3 ± 0.2.

The 3.28 μm intensity profile along the minor axis of the nebula is similar to the 11.3 μm intensity profile of Aitken and Roche (1983), and the FWHP dimensions of the nebula are identical at both wavelengths, ~8″.4. This observed similarity is consistent with suggestions that these UIR features are intimately associated with a single emitting component (Allamandola, Tielens, and Barker 1985; Sakata *et al.* 1984). The peak-to-peak separation at 3.28 μm and 3.4 μm is 6″.2, in good agreement with the 11.3 μm peak-to-peak separation of $5''.8 \pm 0''.2$ observed by Arens *et al.* (1984) and Bentley (1982); however, Aitken and Roche (1983) observe a separation of 7″.2 at 11.3 μm. The difficulty of comparing observations made with different instruments and techniques underscores the importance of our approach of intercomparing images at 3.28 μm, 3.4 μm, and Brα obtained in alternation with the same array detector, to obtain the best spatial registration.

b) UIR Feature Emission and the Continuum Dust Emission

To assess whether the *same* dust component can be responsible for the UIR feature emission at 3.28 μm and 3.4 μm

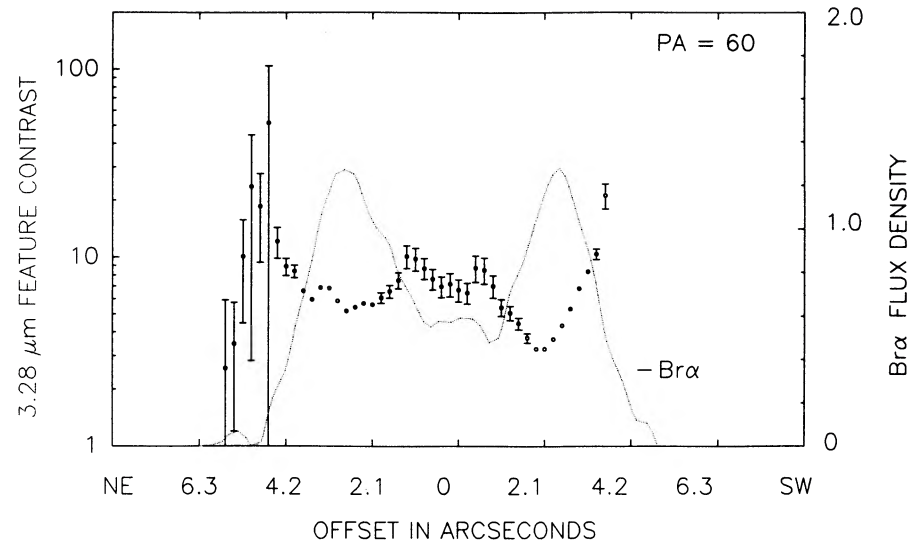

FIG. 3.—Plot of the observed 3.28 μm feature contrast (F[feature]/F[continuum]) along the minor axis (PA = 60°) of NGC 7027. The 3.28 μm continuum intensity is estimated from a weighted linear combination of images taken at adjacent continuum wavelengths. A weak correlation between the feature and continuum is found. For comparison, the continuum-subtracted line-peak Brα (4.052 μm) flux density profile ($\times 4.4 \times 10^{-20}$ W cm^{-2} μm^{-1} arcsec^{-2}) along the same axis is plotted as a dotted line. The error bars represent typical statistical uncertainty ($\pm 1\ \sigma$) in the data.

and the underlying near-infrared continuum emission at wavelengths ~3 μm, we have plotted the 3.28 μm feature contrast (F[feature]/[F[continuum]) as a function of position along the minor axis of the nebula (PA = 60°, Fig. 3). The continuum flux density at 3.28 μm was determined from a weighted linear combination of adjacent continuum images. Overall, there is modest correlation between the 3.28 μm continuum strength and feature strength, unlike the strong correlation found in S106 by Williams and Zealey (1983). A similar result is also found for the 3.4 μm feature and continuum in NGC 7027.

However, close inspection of Figure 3 suggests that there may be two separate, possibly distinct, dust components. Along lines of sight to the central region of the nebula (inner ~4″.1), the feature contrast is fairly flat, varying no more than a factor of 2 (6 ± 2). Toward the edge of the nebula, the feature contrast rises to values in excess of 9. If we assume that the observed feature and continuum emission is proportional to the column depth of emitters along a given line of sight (constant radial density), and if we adopt a simple hollow cylinder geometry for NGC 7027 (see § IIIc below), a rise in the feature contrast can be explained if the UIR emitting material is contained in a shell spatially more extensive than the continuum dust-emitting shell. Indeed, the smaller spatial distribution of the thermally emitting dust component imaged in a broad-band M' filter (Woodward *et al.* 1989*a*) (FWHP[60°] ~ 7″.1 ± 0″.1) as compared to the 3.28 μm UIR feature emission (FWHP[60°] ~ 8″.4 ± 0″.1) lends credence to this interpretation. A two-component dust model also is consistent with the mid-infrared observations of Arens *et al.* (1984) and Bentley (1982).

c) UIR Feature Emission and the Ionized Gas

The most striking result of our observations is that 3.28 μm and 3.4 μm feature emission intensity maxima are exterior to the ionized gas (Table 2; Figs. 4 and 5), indicating that feature emission arises at least partially beyond the H II region/molecular cloud interface. This is especially evident along the minor axis of the nebula (PA = 60°). The larger extent of the 3.28 μm UIR emission is vividly demonstrated in Figure 2 of Woodward *et al.* (1987), a color image showing the 3.28 μm image (in green) overlaid on the Brα image (in red).

The strength of the 3.28 μm emission is moderately correlated with the Brα line flux along the minor axis of the nebula. The 3.28 μm/Brα flux density ratio (Fig. 6) is constant (~1) along much of the minor axis profile, indicating, if the density is constant, that the feature-emitting dust and the ionized gas may be uniformly comixed in the H II region. The rise in the 3.28 μm/Brα ratio at spatial offsets greater than or equal to 3″ from the center of the nebula reflect the result that the regions of highest 3 μm UIR surface brightness are exterior to that of Brα emission (Table 2). The approximate sizes of the shell of the 3.28 μm UIR emission and the ionized gas shell can be estimated by convolving our point spread function (Table 2) with a simple *nonunique* model for NGC 7027.

The observed spatial distributions of the radio (Scott 1973) and mid-infrared emission of NGC 7027 (Bentley 1982) have been successfully modeled using a hollow cylinder. We also will use a one-dimensional cut through two hollow cylinders (axis of the cylinder is perpendicular to the line of sight), where the inner radius, r[in], and outer radius, r[out], of the 3.28 μm and Brα shells are free parameters. Furthermore, the region between the inner and outer radii of the cylinder is assumed to be of *uniform density*. Hence, the intensity of the observed emission will depend only on the column depth along a given line of sight. The model profiles are normalized such that the integrated intensity under the model curve equals that observed.

The fit which best matches (determined from χ^2 minimization) the observed intensity profiles along the minor axis corresponds to a 3.28 μm UIR emission shell with r[in] ~ 3″.3, r[out] ~ 4″.6, and a Brα emission shell with r[in] ~ 2″.6, r[out] ~ 4″.0. The uncertainty in the fits are of order ±0″.1. Comparison of the observed and model 3.28 μm and Brα intensity profiles are given respectively in Figures 7*a* and 7*b*. The poorer model fit to the central regions of the observed intensity profiles indicates that our simple model geometry is not completely adequate. Within the uncertainty, comparable amounts of 3.28 μm emission arise inside and outside the H II region. However, there is clearly an extension of the 3.28 μm emitting

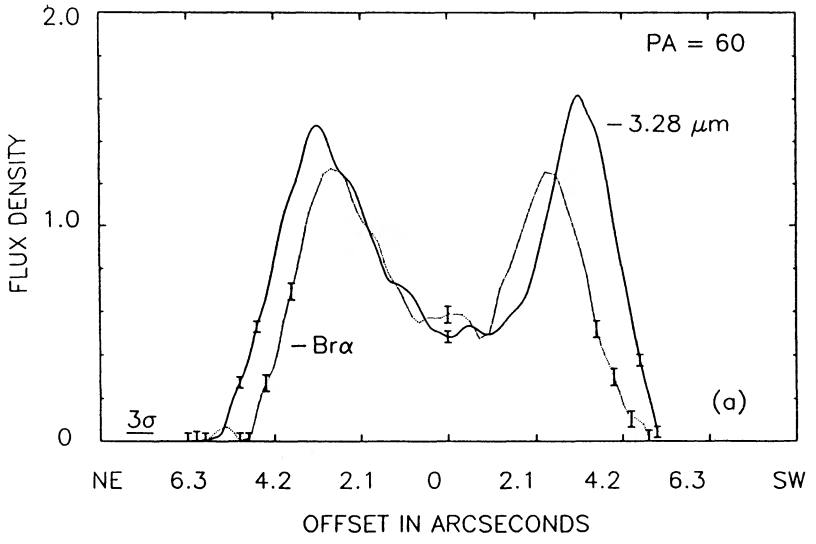

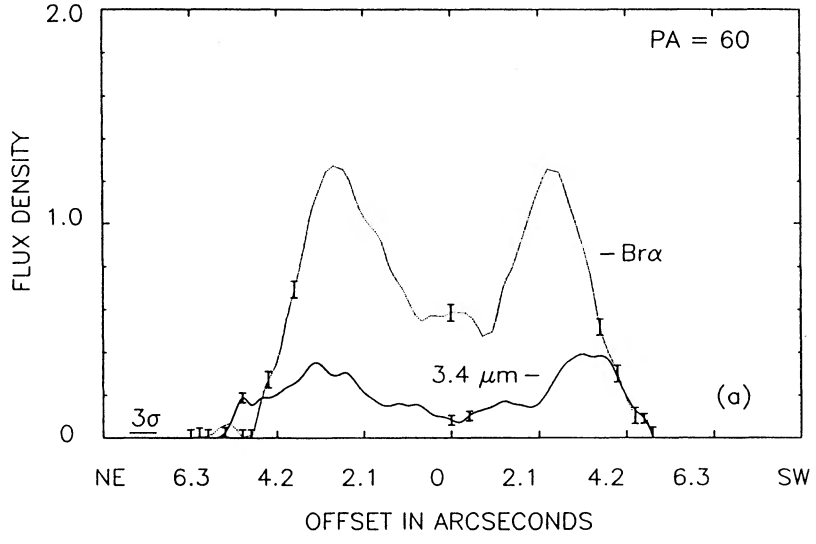

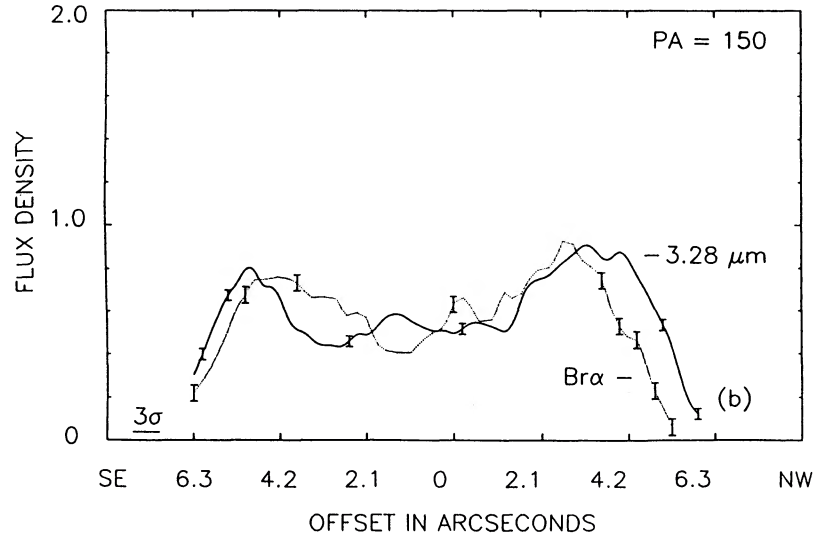

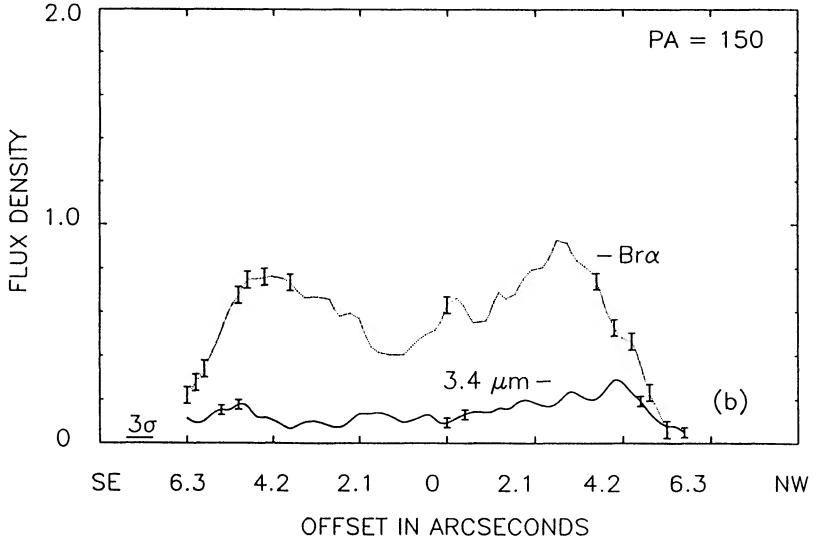

FIG. 4

FIG. 5

FIG. 4.—The continuum-subtracted, feature-peak 3.28 μm flux density and the continuum subtracted, line-peak Brα (4.052 μm) flux density ($\times 4.4 \times 10^{-20}$ W cm^{-2} μm^{-1} arcsec^{-2}) intensity profiles of NGC 7027 from the spectroscopic images obtained on the NASA IRTF 3 m telescope. (*a*) The intensity profiles as a function of position along the minor axis (PA = 60°) on a line passing through the center (0 offset position) of NGC 7027, $\alpha(1950) = 21^h5^m9^s.53$, $\delta(1950) = 42°2'2''.9$. The error bars represent typical statistical uncertainty ($\pm 1\ \sigma$) in the determined continuum subtracted flux densities. (*b*) Same as Fig. 4*a* except along the major axis (PA = 150°). The horizontal bar in lower left of each figure is 3 σ for the Brα flux density.

FIG. 5.—Same as Fig. 4 except the continuum subtracted 3.4 μm feature-peak and the continuum subtracted line-peak Brα (4.052 μm) and flux densities intensity profiles are plotted. The horizontal bar in lower left of each figure is 3 σ for the 3.4 flux density.

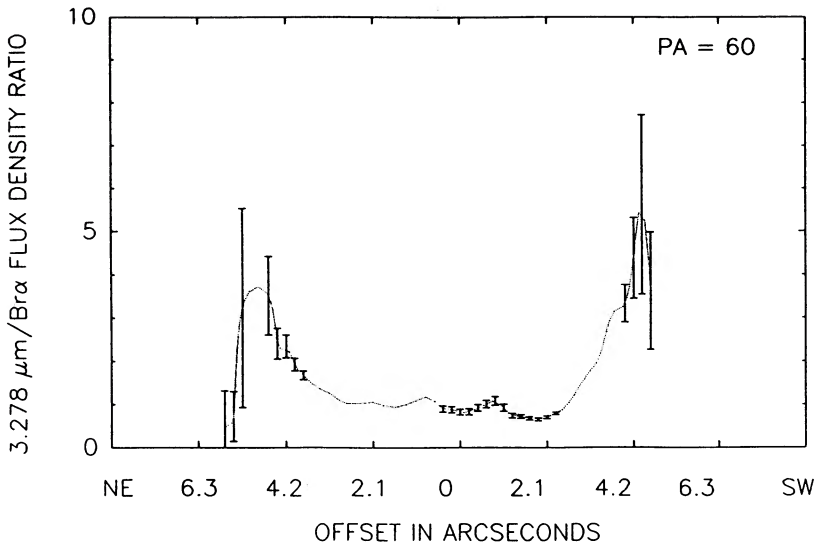

FIG. 6.—The observed 3.28 μm UIR feature flux density/Brα (4.052 μm) line flux density along the minor axis (PA = 60°) of NGC 7027. Typical error bars ($\pm 1\ \sigma$) are indicated by the solid crosses.

UIR region into the neutral zone. Aitken and Roche (1983) find a shell diameter (r[in] $\sim 3''$; r[out] $\sim 4''$) for the 11.3 μm UIR emission.

The inner and outer radii of the UIR emitting shell and the ionized gas shell are dependent on the nature of the assumed density profiles and the geometry. Alternative shell density profiles, $n(r) = n(\max)[r[\text{in}]/r]$ (Atherton *et al.* 1979) and $n(r) = n(\max)[r/r[\text{out}]]$, were also used to model the observed 3.28 μm feature strength and Brα line strength intensity profiles. In these models, the intensity of the gas emission $\propto \int n(e)^2\, dl$, while that of the UIR emission $\propto \int n(d)dl$. These distributions still result in partial overlap of the 3.28 μm and Brα emitting regions, but the resulting derived intensity profiles do not match the observed profiles adequately. However, based on our models, we can rule out both complete overlap and no overlap of the 3.28 μm and Brα emitting regions.

In the context of our simple uniform density model, $\sim 50\%$ of the 3.28 μm UIR emitting volume is exterior to the Brα emission. The precise thickness of the comixed volume of ionized gas and UIR emitting material has not been uniquely determined. However, the interior edge of the 3.28 μm shell lies within the ionized gas and demarcates a location where the UIR emitting component may be destroyed or chemically altered, possibly by the large photon flux (Tielens *et al.* 1987). UIR emitting material clearly exists where the ultraviolet photon radiation field is extremely hard (within the edges of the H II region). Since the H II region expands at ~ 10 km s^{-1} into the surrounding neutral material, the size of the 3.28 μm/Brα overlap region implies a lifetime for the UIR emitting material of a few hundred years.

At the exterior of the 3.28 μm shell (outside the H II region), feature emission ceases when the exciting photons become too heavily attenuated by dust, chemical changes occur in the UIR emitting material (cf. Duley and Williams 1986), or the small grains are destroyed or formed. In NGC 7027, shock processing (Seab and Shull 1985) of large carbon grains in the preexistent red giant envelope may provide the formation mechanism for UIR material (Omont 1986). Indeed the regions of highest surface brightness in H_2 molecular line (2.240 μm) images (Woodward *et al.* 1989*b*), which may be shock excited in NGC 7027 (Thronson 1983; Beckwith *et al.* 1980), lie just exterior to the minor axis (PA = 60°) intensity maxima in the 3.28 μm images.

The number density of UIR emitters, n[PAH], required to account for the total integrated UIR emission in the 3.28 μm band in NGC 7027 can be deduced by comparing the observed 3.28 μm feature luminosity L[3.3] ($\sim 5\ L_\odot$), to the luminosity L[uv] available to excite the UIR features:

$$L[3.3] = \epsilon_{\text{em}}\epsilon_{\text{H}} f_{3.3}\, \sigma[\text{PAH}] l L[\text{uv}] n[\text{PAH}] \Omega/4\pi\ . \quad (1)$$

The efficiency factors ϵ_{em}, the fraction of absorbed photon energy emitted in all of the UIR features by a PAH with full hydrogen coverage, and ϵ_{H}, the additional efficiency factor due to partial hydrogen coverage, respectively, are taken to be unity (i.e., there are no other competing de-excitation channels available to an isolated PAH; Barker *et al.* 1987) and 0.5 (Allamandola, Tielens, and Barker 1985). The fraction of UIR luminosity emitted in the 3.28 μm band compared to the total luminosity in all the 2–13 μm UIR bands, $f_{3.3}$, (~ 0.02) was estimated using the ratio of our observed 3.28 μm luminosity to the sum of the luminosity (assuming a distance of 940 pc) in all other UIR bands, as summarized by Cohen *et al.* (1986). The solid angle $\Omega/4\pi$ is the extent of PAH coverage seen from the exciting star ($\simeq 1.0$), σ[PAH] is the absorption cross section ($\sim 10^{-16}$ cm^2; Tielens *et al.* 1987), and l is the path length ($\sim 1''.3$, cf. Fig. 7) over which both feature emitting grains and exciting photons are available. In equation (1), the ultraviolet luminosity available to excite the feature was taken to be $\simeq 3.6 \times 10^{-8}$ ergs cm^{-2} s^{-1} (Aitken and Roche 1983), for the 2000–4000 Å wavelength range (peak absorption wavelength interval for PAH species; Allamandola, Tielens, and Barker 1985; Birks 1970; Donn 1968).

Thus, we find a number density of UIR emitting grain/molecules, $n(\text{UIR}) \simeq 0.28$ cm^{-3}. Adopting a value of $n(\text{H}) \sim 4 \times 10^4$ cm^{-3} (Beckwith *et al.* 1980), the derived value of n(UIR) indicates that $\simeq 6\%$ (assuming ~ 20 C atoms per average PAH) of the available carbon in NGC 7027 (~ 7 times cosmic abundance; Shields 1978) is locked up in UIR emitting grain/molecules.

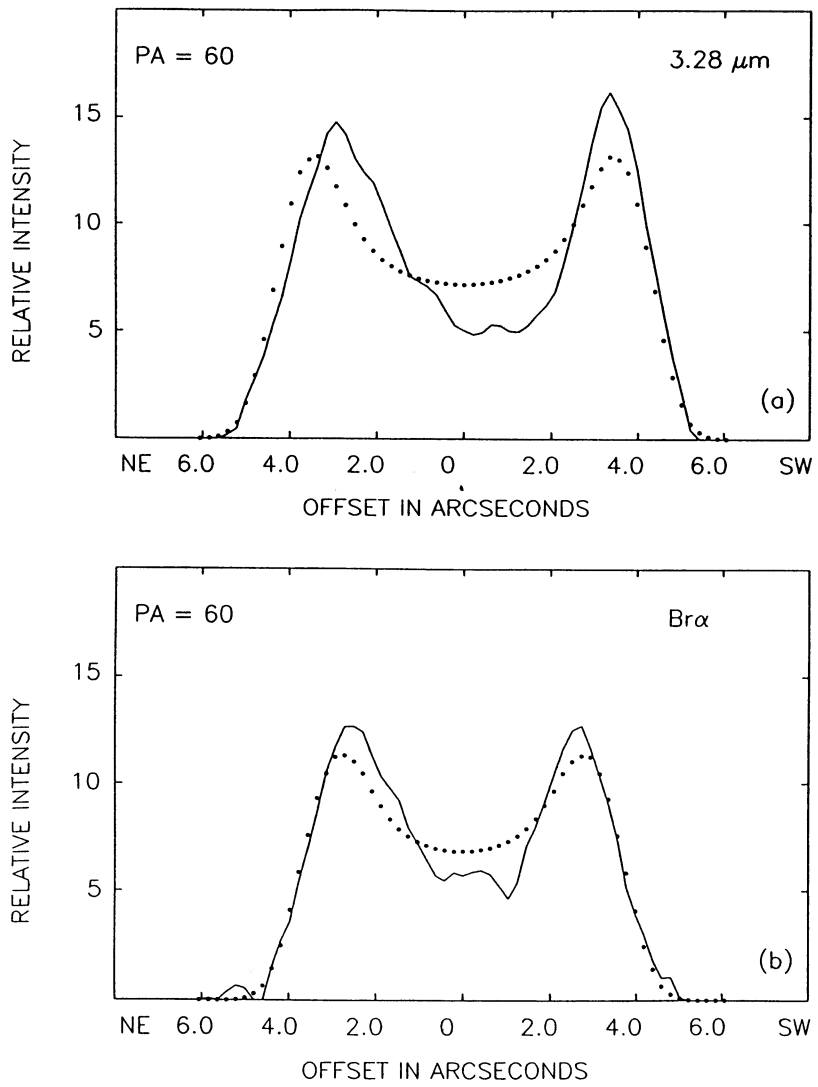

FIG. 7.—Comparison of the observed intensity profiles (*solid curve*) with the best-fit hollow cylinder model intensity profile (*dotted curve*) along the minor axis (PA = 60°) of NGC 7027. (*a*) The 3.28 μm profiles. The fit which best matches the observed intensity profile corresponds to a 3.28 μm UIR emitting shell with r[in] ~ 3.″3 and r[out] ~ 4.″6. (*b*) The Brα profiles. The fit which best matches the observed intensity profile corresponds to a Brα emitting shell with r[in] ~ 2.″6 and r[out] ~ 4.″0. The uncertainty in the model fits are of order ±0.″1.

d) Implications for UIR Emission Models

The observed spatial distributions of the 3.28 μm and 3.4 μm UIR features and their relationships to the ionized gas and continuum dust emission distributions place constraints on the excitation mechanism and possible candidate emitting materials.

Growing theoretical and laboratory evidence suggests that the observed astronomical UIR bands and possibly the near-infrared continuum emission observed to be associated with the UIR features in reflection nebulae (Sellgren, Werner, and Dinerstein 1983) may be attributed to infrared fluorescence from free, highly vibrationally excited polycyclic aromatic hydrocarbon molecules (PAHs) (Allamandola, Tielens, and Barker 1985; Leger and Puget 1984). However, the simple PAH species currently considered as likely candidate carriers of the UIR, such as chrysene, coronene, or circumcoronene (Leger and d'Hendecourt 1987; Allamandola, Tielens, and Barker 1987) may not be able to account for all aspects of the observed spectra of UIR-emitting objects. Donn *et al.* (1987) have pointed out that laboratory spectra of simple PAHs exhibit *no* continuum absorption in the wavelength range between 2 and 5 μm and have a much more complex emission spectrum than that observed in astronomical sources.

In all likelihood, a mixture of PAHs, hydrogenated amorphous carbons, and quenched carbonaceous composites may be needed to explain both the UIR features and the broad underlying continuum emission plateaus seen from 3 to 4 μm (Geballe *et al.* 1985) and 10 to 20 μm (Goebel 1987). For the purposes of our analysis, we will assume that small PAHs are responsible for the UIR emission features and use the theoretical framework outlined by Allamandola, Tielens, and Barker (1987) and Barker, Allamandola, and Tielens (1987).

The relative intensities (specifically the 3.28 μm/3.4 μm ratio) and shapes of the UIR bands in the PAH model are a function of both molecular size and of the internal energy (including the effects of anharmonicity in the vibrational frequencies and energy-cascade from higher vibrational states, $v > 1$) of the

vibrationally excited molecule (Barker, Allamandola, and Tielens 1987). The 3.3 μm/3.4 μm flux ratio deduced from the integrated spectroscopic images is $\sim$6.3 (Table 1). Utilizing Figure 2 of Barker *et al.*, our data suggest that an upper limit to the number of C atoms in the *largest* PAHs present in NGC 7027 is 13–27 for initial vibrational excitation energies of 80,000–100,000 cm^{-1} (for unity conversion this corresponds to exciting photons of wavelengths 1000–1250 Å). We assume, in this analysis, that the 3 μm UIR emission arises from different excitation modes of the same grain.

A similar size range for the UIR emitting species (assuming comparable excitation) is found using 3.28 μm and 3.4 μm feature fluxes measured by Nagata *et al.* (1988) or the 3.28 μm and 11.3 μm integrated band strengths (Cohen *et al.* 1986) and the relative 11.3 μm/3.3 μm UIR intensity ratios derived by Allamandola, Tielens, and Barker (1987). Smaller species of PAHs ($\sim$10 C atoms per molecule; linear chain PAH), with lower vibrational energy content ($\sim$40,000 cm^{-1}; this corresponds to unity conversion of 2500 Å exciting photons, which is in the peak absorption wavelength interval for PAH species) may account for some fraction of the observed UIR emission, especially in the neutral material where less energetic photons are available (see below). The inferred presence of small-sized molecules in this nebula suggests that in this model UIR feature-emission may arise from relatively simple PAHs (chrysene, coronene, circumcorone).

There is significant small-scale spatial variation of the 3.28 μm/3.4 μm flux ratio (Fig. 8) in the nebula. Along this axis of the nebula the 3.28 μm/3.4 μm flux ratio ranges from $\sim$3 to 10. Of most interest, is the *decrease* in the feature ratio (factor of 2) in the northeast quadrant of the nebula from $\sim$7, along lines of sight to the H II region, to a value of $\leq$4, along the line of sight toward neutral material. For a *fixed* initial vibrational excitation energy of 80,000–100,000 cm^{-1}, this observed decrease in the feature ratio implies, in the Barker *et al.* model, a decrease of a factor $\sim$2.5 in the average number of C atoms in a PAH.

However, one expects the UV photon energy to be lower in the neutral material outside the ionization front. If the exciting photon energy varies by a factor of 2 across the ionization front (e.g., 100,000–80,000 cm^{-1} to 40,000 cm^{-1}), the observed decrease in the 3.28 μm/3.4 μm feature ratio cannot be explained by the Barker *et al.* model. For initial vibrational energies of $\sim$40,000 cm^{-1}, and an observed feature ratio of $\sim$4, the number of C atoms in an emitting PAH becomes extremely small, $\sim$6. The *smallest* PAH ring (benzene, C_6H_6) requires six carbon atoms.

Estimates of the PAH molecular size discussed above are mildly sensitive to uncertainties in the derived feature flux ratios due to uncertainties in the appropriate continuum level to subtract, as discussed in § II. We estimate an uncertainty in the flux ratio of $\sim$20%, due mostly in the uncertainty in the appropriate 3.4 μm continuum. Furthermore, we assume the widths of the 3.28 μm to 3.4 μm UIR features do not vary along different lines of sight. In part, this assumption is justified by the results of Geballe *et al.* (1985) who find that the 3.28 μm and 3.4 μm feature-widths are roughly constant (in μm) in a wide variety of objects with dissimilar excitation conditions. However, in NGC 7027 a variation of $\sim$50% in the 11.3 μm feature width is evident in the spectrum obtained along the line of sight toward the ionized zone versus that toward neutral zone (Aitken and Roche 1983). Similar spatially resolved, high-resolution spectra near the 3 μm UIR features along differing lines of sight toward NGC 7027 have not been published in the literature.

IV. CONCLUSIONS

Spectroscopic images of the 3 μm UIR features in NGC 7027 clearly show that the feature emission is more extensive than that of the ionized gas, with strong emission still evident along lines of sight to the neutral zone. Modeling the spatial distribution of the UIR and Brα emission suggests that the UIR feature emitting region overlaps into the H II region. Based on these observations and our *nonunique* model for the nebula we find: (1) nonionizing photons can excite the 3.28 μm UIR feature; and (2) the inner cutoff of the 3.28 μm emission within the ionized region may be the result of destruction of UIR emitting

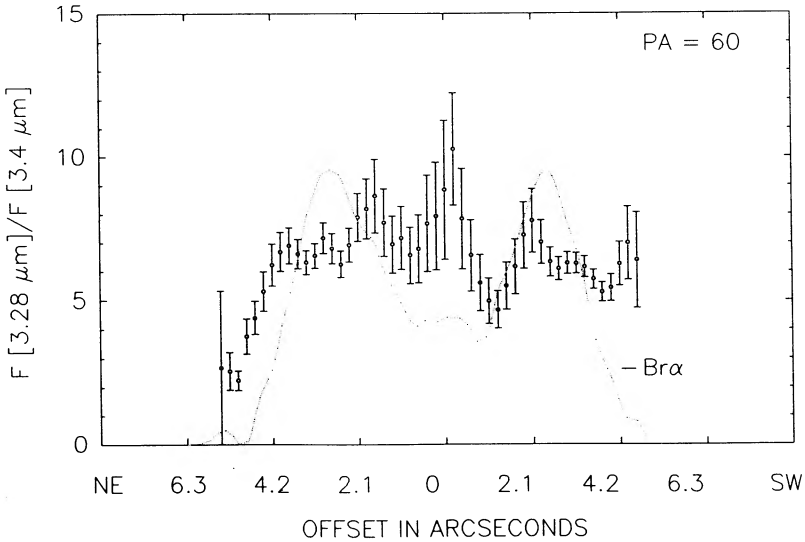

FIG. 8.—The 3.28 μm/3.4 μm flux ratio as a function of position along the minor axis (PA = 60°) of NGC 7027. For comparison, the continuum-subtracted line-peak Brα (4.052 μm) flux density profile (arbitrary units) along the same axis is plotted as a dotted line. Typical error bars ($\pm 1\ \sigma$) are indicated by the solid crosses.

material caused by the large ultraviolet photon number density. Shock processing (Seab and Shull 1985) of the UIR emitting grains or reactions with atoms (Duley and Williams 1986) may provide the mechanism for the chemical/physical change in the feature-emitting material at the outer boundary of the 3.28 μm emission in the neutral region.

This research was supported by NSF contract AST-8318651 and a National Geographic Society grant 2932-84 (University of Rochester). C. E. Woodward also acknowledges the support of the University of Wyoming (Air Force contract AFSOR-85-0058) where this paper was written. K. Sellgren is supported by NASA contract NASW-3159.

REFERENCES

Aitken, D. K., and Roche, P. F. 1983, *M.N.R.A.S.*, **202**, 1233.
Allamandola, L. J., Tielens, A. G. G. M., and Barker, J. R. 1985, *Ap. J. (Letters)*, **290**, L25.
———. 1987, in *Polycyclic Aromatic Hydrocarbons and Astrophysics*, ed. A. Leger and L. B. Henedecourt (Dordrecht: Reidel), p. 255.
Arens, J. F., Lamb, G. M., Peck, M. C., Moseley, H., Hoffman, W. F., Tresch-Fienberg, R., and Fazio, G. G. 1984, *Ap. J.*, **279**, 685.
Atherton, P. D., Hicks, T. R., Reay, N. K., Robinson, G. J., and Worswick, S. P. 1979, *Ap. J.*, **232**, 786.
Barker, J. R., Allamandola, L. J., and Tielens, A. G. G. M. 1987, *Ap. J. (Letters)*, **315**, L61.
Beckwith, S., Neugebauer, G., Becklin, E. E., and Matthews, K. 1980, *A.J.*, **85**, 886.
Bentley, A. F. 1982, *A.J.*, **87**, 1810.
Birks, J. B. 1970, *Photophysics of Aromatic Molecules* (London: Wiley–Interscience).
Borghesi, A., Bussoletti, E., and Colangeli, L. 1987, *Ap. J.*, **314**, 442.
Brocklehurst, M. 1971, *M.N.R.A.S.*, **153**, 471.
Cohen, M., Allamandola, L., Tielens, A. G. G. M., Bregman, J., Simpson, J. P., Witteborn, F. C., Wooden, D., and Rank, D. 1986, *Ap. J.*, **302**, 737.
Cudworth, K. M., and Orvecz, M. 1978, *Pub. A.S.P.*, **90**, 333.
d'Hendecourt, L., Leger, A., Olofsson, G., and Schmidt, W. 1986, *Astr. Ap.*, **170**, 91.
Donn, B. 1968, *Ap. J. (Letters)*, **152**, L129.
Duley, W. W., and Williams, D. A. 1986, *M.N.R.A.S.*, **219**, 859.
Forrest, W. J., Moneti, A., Woodward, C. E., Pipher, J. L., and Hoffman, A. 1985, *Pub. A.S.P.*, **97**, 183.
Forrest, W. J., Pipher, J. L., and Stein, W. A. 1986, *Ap. J. (Letters)*, **301**, L49.
Geballe, T. R., Lacy, J. H., Persson, S. E., McGregor, P. J., and Soifer, B. T. 1985, *Ap. J.*, **292**, 500.
Giles, K. 1977, *M.N.R.A.S.*, **180**, 57P.
Goebel, J. H. 1987, in *Polycyclic Aromatic Hydrocarbons and Astrophysics*, ed. A. Leger and L. B. Henedecourt (Dordrecht: Reidel), p. 329.
Leger, A., and d'Hendecourt, L. B. 1987, in *Polycyclic Aromatic Hydrocarbons and Astrophysics*, ed. A. Leger and L. B. Henedecourt (Dordrecht; Reidel), p. 223.
Leger, A., and Puget, J. L. 1984, *Astr. Ap.*, **137**, L5.
Masson, C. R. 1986, *Ap. J. (Letters)*, **302**, L27.
Merrill, K. M., Soifer, B. T., and Russell, R. W. 1975, *Ap. J. (Letters)*, **200**, L37.
Nagata, T., Tokunaga, A., Sellgren, K., Smith, R. G., Onaka, T., Nakada, Y., and Sakata, A. 1988, *Ap. J.*, **326**, 157.
Natta, A., and Panagia, N. 1981, *Ap. J.*, **248**, 189.
Omont, A. 1986, *Astr. Ap.*, **164**, 159.
Sakata, A., Wada, S., Tanabe, T., and Onaka, T. 1984, *Ap. J. (Letters)*, **287**, L51.
Scott, P. F. 1973, *M.N.R.A.S.*, **161**, 35P.
Seab, C. G., and Shull, J. M. 1985, *Ap. J.*, **275**, 652.
Sellgren, K., Werner, M. W., and Dinerstein, H. L. 1983, *Ap. J. (Letters)*, **271**, L13.
Shields, G. 1978, *Ap. J.*, **219**, 565.
Thronson, H. A. 1983, *Ap. J.*, **262**, 599.
Tielens, A. G. G. M., Allamandola, L. J., Barker, J. R., and Cohen, M. 1987, in *Polycyclic Aromatic Hydrocarbons and Astrophysics*, ed. A. Leger and L. B. Henedecourt (Dordrecht: Reidel), p. 273.
Williams, P. M., and Zealey, W. J. 1983, *M.N.R.A.S.*, **203**, 433.
Woodward, C. E. 1987, Ph.D. thesis, University of Rochester.
Woodward, C. E., Pipher, J. L., Moneti, A., Shure, M., and Forrest, W. J. 1989*a*, in preparation.
Woodward, C. E., Pipher, J. L., Shure, M., and Sellgren, K. 1989*b* in preparation.
Woodward, C. E., Pipher, J. L., Shure, M., Forrest, W. J., Sellgren, K., and Nagata, T. 1987, in *Proc. of the Workshop on Ground-based Astronomical Observations with Infrared Array Detectors*, ed. C. G. Wynn-Williams and E. E. Becklin (Honolulu: University of Hawaii), p. 299.

W. J. FORREST and J. L. PIPHER: Department of Physics and Astronomy, University of Rochester, Rochester, NY 14607

K. SELLGREN and M. A. SHURE: Institute for Astronomy, University of Hawaii at Manoa, 2680 Woodlawn Drive, Honolulu, HI 96822

C. E. WOODWARD: Wyoming Infrared Observatory, Department of Physics and Astronomy, P.O. Box 3905, University Station, University of Wyoming, Laramie, WY 82071